

One-component fermion plasma on a sphere at finite temperature

Riccardo Fantoni

*Dipartimento di Fisica, Università di Trieste
Strada Costiera 11, 34151 Grignano (Trieste), Italy
rfantoni@ts.infn.it*

Received 1 May 2018

Accepted 5 June 2018

Published 11 July 2018

We study through a computer experiment, using the restricted path integral Monte Carlo method, a one-component fermion plasma on a sphere at finite, nonzero, temperature. We extract thermodynamic properties like the kinetic and internal energy per particle and structural properties like the radial distribution function. This study could be relevant for the characterization and better understanding of the electronic properties of hollow graphene spheres.

Keywords: One-component plasma; hollow graphene sphere; Monte Carlo simulation; finite temperature; restricted path integral; worm algorithm; fermions sign problem; structure; radial distribution function; thermodynamics; internal energy.

PACS Nos.: 02.70.Ss, 05.10.Ln, 05.30.Fk, 05.70.-a, 61.20.Ja, 61.20.Ne.

1. Introduction

We want to study the one-component fermion plasma on the surface of a sphere of radius a at finite, nonzero, temperature, as an evolution of the Thomson problem. The plasma is an ensemble of point-wise electrons which interact through the Coulomb potential assuming that the electric field lines can permeate the tridimensional space where the sphere is embedded. The system of particles is thermodynamically stable even if the pair-potential is purely repulsive because the particles are confined to the compact surface of the sphere, and we do not need to add a uniform neutralizing background as in the Wigner *Jellium* model. Therefore, our spherical plasma made of N spinless indistinguishable electrons of charge $-e$ and mass m will carry a total negative charge $-Ne$, a total mass Nm , and will have a radius a .

Note that in the limit $a \rightarrow \infty$ with a fixed surface density $\sigma = N/4\pi a^2$ our system becomes thermodynamically unstable since all the particles tend to escape to infinity. In order to prevent this pathological scenario one would have to add a uniform neutralizing background on the spherical surface of positive surface charge density $+\sigma e$. This amounts to replacing the Coulomb potential e^2/r with the corrected one

$e^2/r - B$ with $B = \int_{\text{sphere}} (e^2/r) dA / (4\pi a^2) = e^2$, where the integral is over the surface of the sphere $dA = a^2 \sin \theta d\theta d\varphi$ and $r = a\sqrt{2 - 2\cos\theta}$ is the Euclidean distance between the north pole and another point on the sphere, with polar angle θ . The constant D is chosen to make sure that the average value of the interaction is zero and must be subtracted from the self-energy which would otherwise be zero. We would then obtain the Wigner Jellium system on the sphere which has received much attention from the point of view of path integral Monte Carlo recently in the Euclidean tridimensional space.¹⁻⁸

We want to study the structural and thermodynamic properties at finite, nonzero, temperature of the spherical fermion plasma through restricted path integral Monte Carlo. In particular, we will calculate the radial distribution function of the particles on the surface of the sphere and their kinetic and internal energy per particle.

Even if impenetrable identical particles on the surface of a sphere admit a fractional anyonic statistics,⁹ we will just study their fermionic nature, leaving the implementation of the anyonic statistics to a subsequent work. This amounts to distinguishing only among even and odd permutations rather than among the larger elements of the braid group. We will then consider the union of all the topologically disjoint portions of the particles configuration space belonging just to each of the two fermionic sections. This simplifies the problem considerably since the braid group is much larger and complex than the permutation group.⁹

A quantum fluid on a Riemannian surface has been studied before in relation to the quantum Hall effect.¹⁰⁻¹² A generalized stochastic method has also been implemented for the many-body ground state.^{13,14} We are not aware of any path integral Monte Carlo attempt in the spirit of our work. We expect our work to be relevant for the characterization of the electronic properties of hollow graphene spheres^{15,16} constructed in the laboratory and for their implementation as electrodes for supercapacitors and batteries, as superparamagnetic materials, as electrocatalysts for oxygen reduction, as drug deliverers, and as a conductive catalyst for photovoltaic applications.¹⁷⁻²⁵ Our numerical experiments, albeit idealized, are capable of exploring the properties of these systems under the most various thermodynamic conditions, even extreme conditions otherwise not accessible in the laboratory. Therefore we are able to explore and characterize the phenomenology of these systems with cost-free computer experiments that can later be used as guides for the laboratory set up.

The paper is organized as follows: in Sec. 2, we describe the problem we want to solve and the method used for its resolution, in Sec. 3, we present our numerical results, and Sec. 4 is for the concluding discussion.

2. The Problem

A point \mathbf{q} on the sphere of radius a , the surface of constant positive curvature, is given by

$$\mathbf{r}/a = \sin \theta \cos \varphi \hat{\mathbf{x}} + \sin \theta \sin \varphi \hat{\mathbf{y}} + \cos \theta \hat{\mathbf{z}}, \quad (1)$$

with θ the polar angle and φ the azimuthal angle. The N particles positions are at $\mathbf{R} = (\mathbf{r}_1, \mathbf{r}_2, \dots, \mathbf{r}_N)$. The surface density of the plasma will then be $\sigma = N/4\pi a^2$. On the sphere we have the following metric:

$$ds^2 = g_{\mu\nu} dq^\mu dq^\nu = a^2 [d\theta^2 + \sin^2 \theta d\varphi^2], \quad (2)$$

where Einstein summation convention on repeated indices is assumed, we will use Greek indices for either the surface components or the surface components of each particle coordinate and roman indices for either the particle index or the time-slice index, $q^1 = \theta \in [0, \pi)$, $q^2 = \varphi \in [-\pi, \pi)$, and the positive definite and symmetric metric tensor is given by

$$g_{\mu\nu} = \begin{pmatrix} a^2 & 0 \\ 0 & a^2 \sin^2 \theta \end{pmatrix}. \quad (3)$$

We have periodic boundary conditions in $\theta + \pi = \theta$ and in $\varphi + 2\pi = \varphi$. We will not need to implement explicitly the periodic boundary conditions as all that is needed in the simulation is the geodesic and the Euclidean distance which are expressed in terms of trigonometric functions which are periodic in the coordinates θ and φ . We will also define $\mathbf{Q} = (\mathbf{q}_1, \mathbf{q}_2, \dots, \mathbf{q}_N)$ which will be the coordinates used in the code. The geodesic distance between two infinitesimally close points \mathbf{Q} and \mathbf{Q}' is $ds^2(\mathbf{Q}, \mathbf{Q}') = \sum_{i=1}^N ds^2(\mathbf{q}_i, \mathbf{q}'_i)$, where the geodesic distance between the points \mathbf{q} and \mathbf{q}' on the sphere is

$$s(\mathbf{q}, \mathbf{q}') = a \arccos[\cos(q^1) \cos(q^{1'})] \quad (4)$$

$$+ \sin(q^1) \sin(q^{1'}) \cos(q^2 - q^{2'}). \quad (5)$$

On a computer the haversine formula is numerically better conditioned for small distances. Moreover, to avoid rounding errors for the special case of antipodal points the Vincenty formula for an ellipsoid with equal major and minor axes may be used.

The Hamiltonian of the N nonrelativistic indistinguishable particles of the one-component spinless fermion plasma is given by

$$\mathcal{H} = \mathcal{T} + \mathcal{V} = -\lambda \sum_{i=1}^N \Delta_i + \sum_{i<j} v_{ij}, \quad (6)$$

with $\lambda = \hbar^2/2m$, where m is the electron mass, and $\Delta_i = g_i^{-1/2} \partial(g_i^{1/2} g_i^{\mu\nu} \partial/\partial q_i^\nu)/\partial q_i^\mu$ the Laplace–Beltrami operator for the i th particle on the sphere of radius a in local coordinates, where $g_{\mu\alpha} g^{\alpha\nu} = \delta_\mu^\nu$ and $g_i = \det ||g_{\mu\nu}(\mathbf{q}_i)||$. We have assumed that \mathcal{H} in curved space has the same form as in flat space. For the pair-potential, v , we will choose

$$v_{ij} = e^2/r_{ij}, \quad (7)$$

where e is the electron charge and r_{ij} is the Euclidean distance between two particles at \mathbf{q}_i and \mathbf{q}_j , which is given by

$$r_{ij} = a \sqrt{2 - 2\hat{\mathbf{r}}_i \cdot \hat{\mathbf{r}}_j} = 2a \sin[\arccos(\hat{\mathbf{r}}_i \cdot \hat{\mathbf{r}}_j)/2], \quad (8)$$

where $\hat{\mathbf{r}}_i = \mathbf{r}_i/a$ is the versor that from the center of the sphere points towards the center of the i th particle.

Given the antisymmetrization operator \mathcal{A} , and the inverse temperature $\beta = 1/k_B T$, with k_B Boltzmann's constant, the one-component fermion plasma density matrix, $\rho_F = \mathcal{A}e^{-\beta\mathcal{H}}$, in the coordinate representation, on a generic Riemannian manifold of metric g ,^{26,27} is

$$\rho_F(\mathbf{Q}', \mathbf{Q}; \beta) = \int \rho_F(\mathbf{Q}', \mathbf{Q}((M-1)\tau); \tau) \cdots \rho_F(\mathbf{Q}(\tau), \mathbf{Q}; \tau) \times \prod_{j=1}^{M-1} \sqrt{\tilde{g}_{(j)}} \prod_{i=1}^N dq_i^1(j\tau) \wedge dq_i^2(j\tau), \quad (9)$$

where as usual we discretize the *imaginary thermal time* in bits $\tau = \hbar\beta/M$. We will often use the following shorthand notation for the *path integral* measure: $\prod_{j=1}^{M-1} \sqrt{\tilde{g}_{(j)}} \prod_{i=1}^N dq_i^1(j\tau) \wedge dq_i^2(j\tau) \rightarrow \mathcal{D}\mathbf{Q}$ as $M \rightarrow \infty$. The path of the i th particle is given by $\{\mathbf{q}_i(t)|t \in [0, \hbar\beta]\}$ with t the imaginary thermal time. Each $\mathbf{q}_i(j\tau)$ with $i = 1, \dots, N$ and $j = 1, \dots, M$ represents the various *beads* forming the discretized path. The N particle path is given by $\{\mathbf{Q}(t)|t \in [0, \hbar\beta]\}$. Moreover,

$$\tilde{g}_{(j)} = \det \|\tilde{g}_{\mu\nu}(\mathbf{Q}(j\tau))\|, \quad j = 1, 2, \dots, M-1, \quad (10)$$

$$\tilde{g}_{\mu\nu}(\mathbf{Q}) = g_{\alpha_1\beta_1}(\mathbf{q}_1) \otimes \cdots \otimes g_{\alpha_N\beta_N}(\mathbf{q}_N). \quad (11)$$

In the small τ limit we have

$$\rho_F(\mathbf{Q}(2\tau), \mathbf{Q}(\tau); \tau) = (2\pi\hbar)^{-N} \mathcal{A}[\tilde{g}_{(2)}^{-1/4} \sqrt{D(\mathbf{Q}(2\tau), \mathbf{Q}(\tau); \tau)} \tilde{g}_{(1)}^{-1/4} \times e^{\lambda R(\mathbf{Q}(\tau))/6\hbar} e^{-\frac{1}{\hbar}S(\mathbf{Q}(2\tau), \mathbf{Q}(\tau); \tau)}], \quad (12)$$

where \mathcal{A} can act on the first, or on the second, or on both *time slices*, $R(\mathbf{Q})$ the scalar curvature of the curved manifold, S the action and D the van Vleck's determinant

$$D_{\mu\nu} = -\frac{\partial^2 S(\mathbf{Q}(2\tau), \mathbf{Q}(\tau); \tau)}{\partial Q^\mu(2\tau) \partial Q^\nu(\tau)}, \quad (13)$$

$$\det \|D_{\mu\nu}\| = D(\mathbf{Q}(2\tau), \mathbf{Q}(\tau); \tau), \quad (14)$$

where the Greek index denotes the two components of each particle coordinate.

For the *action* and the *kinetic-action* we have

$$S(\mathbf{Q}', \mathbf{Q}) = K(\mathbf{Q}', \mathbf{Q}) + U(\mathbf{Q}', \mathbf{Q}), \quad (15)$$

$$K(\mathbf{Q}', \mathbf{Q}) = \frac{3N\hbar}{2} \ln(4\pi\lambda\tau/\hbar) + \frac{\hbar^2 s^2(\mathbf{Q}', \mathbf{Q})}{4\lambda\tau}, \quad (16)$$

where in the *primitive approximation*²⁸ we find the following expression for the *interaction*,

$$U(\mathbf{Q}', \mathbf{Q}) = \frac{\tau}{2} [V(\mathbf{Q}') + V(\mathbf{Q})], \quad (17)$$

$$V(\mathbf{Q}) = \sum_{i < j} v_{ij}. \quad (18)$$

In particular, the kinetic-action is responsible for a diffusion of the random walk with a variance of $2\lambda\tau g^{\mu\nu}/\hbar$.

On the sphere we have $R = N\mathcal{R}$ with $\mathcal{R} = 2/a^2$, the scalar curvature of the sphere of radius a , and in the $M \rightarrow \infty$ limit $s(\mathbf{Q}', \mathbf{Q}) \rightarrow ds(\mathbf{Q}', \mathbf{Q})$ and $\tilde{g}_{(2)}^{-1/4} \sqrt{D(\mathbf{Q}(2\tau), \mathbf{Q}(\tau); \tau)} \tilde{g}_{(1)}^{-1/4} \rightarrow (\hbar^2/2\lambda\tau)^N$. We recover the Feynman–Kac path integral formula on the sphere in the $\tau \rightarrow 0$ limit. In a computer experiment calculation it is enough to take M sufficiently large, of the order of 100 or 1000,²⁸ so to keep $\tau \sim 0.01$, recalling the primitive approximation error scales as $\sim \lambda\tau^2$. We will then have to deal with $2NM$ multidimensional integrals for which Monte Carlo is a suitable computational method. For example to measure an observable \mathcal{O} we need to calculate the following quantity:

$$\langle \mathcal{O} \rangle = \frac{\int O(\mathbf{Q}, \mathbf{Q}') \rho_F(\mathbf{Q}', \mathbf{Q}; \beta) d\mathbf{Q} d\mathbf{Q}'}{\int \rho_F(\mathbf{Q}, \mathbf{Q}; \beta) d\mathbf{Q}}, \quad (19)$$

where $\sqrt{\tilde{g}} \prod_{i=1}^N dq_i^1 \wedge dq_i^2 \equiv d\mathbf{Q}$. Note that most of the properties that we will measure are diagonal in coordinate representation, requiring then just the diagonal density matrix, $\rho_F(\mathbf{Q}, \mathbf{Q}; \beta)$. For example, for the radial distribution function, $g(r) = \langle \mathcal{O} \rangle$ with r the Euclidean distance between points \mathbf{q} and \mathbf{q}' , $r = 2a \sin[\arccos(\hat{\mathbf{q}} \cdot \hat{\mathbf{q}}')/2]$, we have the following histogram estimator:

$$O(\mathbf{Q}; r) = \sum_{i \neq j} \frac{1_{[r-\Delta/2, r+\Delta/2]}(q_{ij})}{N n_{id}(r)}, \quad (20)$$

where Δ is the histogram bin, $1_{[a,b]}(x) = 1$ if $x \in [a, b[$ and 0 otherwise, and

$$n_{id}(r) = N \left[\left(\frac{r + \Delta/2}{2a} \right)^2 - \left(\frac{r - \Delta/2}{2a} \right)^2 \right], \quad (21)$$

is the average number of particles on the spherical crown $[r - \Delta/2, r + \Delta/2[$ for the ideal gas of density σ . We have that $\sigma^2 g(r)$ gives the probability that sitting on a particle at \mathbf{q} one has to find another particle at \mathbf{q}' .

Fermions' properties cannot be calculated exactly with path integral Monte Carlo because of the fermions sign problem.^{29,30} We then have to resort to an approximated calculation. The one we chose was the restricted path integral approximation^{29,30} with a “free fermions restriction”. The trial density matrix used in the restriction is chosen as the one reducing to the ideal density matrix in the limit of $t \ll 1$ and is given by

$$\rho_0(\mathbf{Q}', \mathbf{Q}; t) \propto \mathcal{A} \left\| e^{-\frac{\hbar s^2(\mathbf{q}', \mathbf{q}_j)}{4\lambda t}} \right\|. \quad (22)$$

The *restricted path integral identity* that we will use states^{29,30}

$$\rho_F(\mathbf{Q}', \mathbf{Q}; \beta) \propto \int \sqrt{\tilde{g}''} d\mathbf{Q}'' \rho_F(\mathbf{Q}'', \mathbf{Q}; 0) \quad (23)$$

$$\times \oint_{\mathbf{Q}'' \rightarrow \mathbf{Q}' \in \gamma_0(\mathbf{Q})} \mathcal{D}\mathbf{Q}''' e^{-S[\mathbf{Q}''']/\hbar},$$

where S is the Feynman–Kac action.

$$S[\mathbf{Q}] = \int_0^{\hbar\beta} dt \left[\frac{\hbar^2}{4\lambda} \dot{\mathbf{Q}}_\mu \dot{\mathbf{Q}}^\mu + V(\mathbf{Q}) \right]. \quad (24)$$

Here, the dot indicates a total derivative with respect to the imaginary thermal time, and the subscript in the path integral of Eq. (2) means that we restrict the path integration to paths starting at \mathbf{Q}'' , ending at \mathbf{Q}' and avoiding the nodes of ρ_0 , that is *the reach of \mathbf{Q}* . The nodes are on the reach boundary $\partial\gamma_0$. The weight of the walk is $\rho_F(\mathbf{Q}'', \mathbf{Q}; 0) = \mathcal{A}\delta(\mathbf{Q}'' - \mathbf{Q}) = (N!)^{-1} \sum_{\mathcal{P}} (-)^{\mathcal{P}} \delta(\mathbf{Q}'' - \mathcal{P}\mathbf{Q})$, where the sum is over all the permutations \mathcal{P} of the N fermions, $(-)^{\mathcal{P}}$ is the permutation sign, positive for an even permutation and negative for an odd permutation, and the Dirac’s delta function is on the sphere. It is clear that the contribution of all the paths for a single element of the density matrix will be of the same sign, thus solving the sign problem; positive if $\rho_F(\mathbf{Q}'', \mathbf{Q}; 0) > 0$, negative otherwise. On the diagonal the density matrix is positive and on the path restriction $\rho_F(\mathbf{Q}', \mathbf{Q}; \beta) > 0$, then only even permutations are allowed since $\rho_F(\mathbf{Q}, \mathcal{P}\mathbf{Q}; \beta) = (-)^{\mathcal{P}} \rho_F(\mathbf{Q}, \mathbf{Q}; \beta)$. It is then possible to use a bosons calculation to get the fermions case. Clearly the restricted path integral identity with the free fermions restriction becomes exact if we simulate free fermions, but otherwise is just an approximation. The approximation is expected to become better at low density and high temperature, i.e. when correlation effects are weak. The implementation of the restricted, fixed nodes, path integral identity within the worm algorithm has been the subject of a recent study on the tridimensional Euclidean Jellium.

We will use the *worm algorithm*^{31,32} to generate spontaneously the needed permutations for the antisymmetrization operator \mathcal{A} . The permutations on the sphere will generate paths with different braiding properties. Identical impenetrable (scalar) particles on a sphere are, in general, anyons with fractional statistics.⁹ Here we will just project out the fermionic component of the broader braid group by just looking at the sign of the trial free fermions density matrix. The object of study is still the realization of the simulation of the anyonic system. The worm algorithm is able to sample the necessary permutations of the indistinguishable particles without the need of explicitly sampling the permutations space treating the paths as “worms” with a tail (*Masha*) and a head (*Ira*) in the β -periodic imaginary time, which can be attached one with the other in different ways or swap some of their portions.

We will work in the grand canonical ensemble with fixed chemical potential μ , surface area $A = 4\pi a^2$, and absolute temperature T . At a higher value of the

chemical potential we will have a higher number of particles on the surface and a higher density. On the other hand, increasing the radius of the sphere at constant chemical potential will produce a plasma with lower surface density. The *Coulomb coupling constant* is $\Gamma = \beta e^2 / a_0 r_s$ with $a_0 = \hbar^2 / m e^2$ the Bohr radius and $r_s = (4\pi\sigma)^{-1/2} / a_0$. At weak coupling, $\Gamma \ll 1$, the plasma becomes weakly correlated and approaches the ideal gas limit. This will occur at high temperature and/or low density. The *electron degeneracy parameter* is $\Theta = T / T_D$, where the degeneracy temperature $T_D = \sigma \hbar^2 / m k_B$. For temperatures higher than T_D , $\Theta \gg 1$, quantum effects are less relevant.

3. Results

Choosing length in Wigner–Seitz’s radius, $a_0 r_s$, units and energies in Rydberg’s, $\text{Ry} = \hbar^2 / 2 m a_0^2$, units we have $\lambda = \text{Ry} / r_s^2$, $\Gamma = \beta (2 / r_s)$, and $\Theta = (2\pi r_s^2) / \beta$. We then see immediately that when quantum effects are relevant, at $\Theta \lesssim 1$, and at low density or high r_s the potential energy dominates in the Hamiltonian (6) and the electron plasma tends to crystallize in a Wigner’s crystal. On the other hand at $\Theta \gg 1$, in the classical regime, the system tends to crystallize at high density. In our grand canonical simulation it is rather convenient to choose the length unit to be just the Bohr radius since r_s is not an input parameter.

We use a free fermion trial density matrix restriction for the fixed nodes path integral calculation from the worm algorithm^{32,33} to the reach of the reference point in moves ending in the Z sector: remove, close, wiggle, and displace. We will use the primitive approximation of Eq. (17). Our algorithm has been recently described in Ref. 34. Here we do not randomize the reference point time slice and we do not restrict the G sector. We choose the probability of being in the G sector ($\propto C_0$ in Ref. 32) so as to have Z sector’s acceptance ratio close to 8/10. The restriction implementation is rather simple: we just reject the move whenever the proposed path is such that the ideal fermion density matrix (22) calculated between the reference point and any of the time slices subject to newly generated particles positions has a negative value. The algorithm will spontaneously choose the optimal needed τ , in the sense that for bigger τ it will not be able to come back and forth between the Z and the G sector remaining stuck in the G sector.

The restricted worm algorithm simulations length was $n \times 10^3$ blocks, with $n \in [0, 10]$ an integer. Each block was made of 500 steps during which 100 moves were made and measures and averages taken. The moves were of nine kinds: advance, recede, insert, open and swap ending in the G sector; remove, close, wiggle and displace ending in the Z sector.³⁵ Each move involved no more than 20 time slices. And they were chosen from a menu with equal probabilities. The integration measures factors \sqrt{g} were only used in the acceptance probabilities of the self-complementary moves: wiggle, swap and displace.

In Table 1 we show the cases studied in our simulations. The first case A is at a temperature of about 3946 K below the graphene melting temperature.³⁶ From the

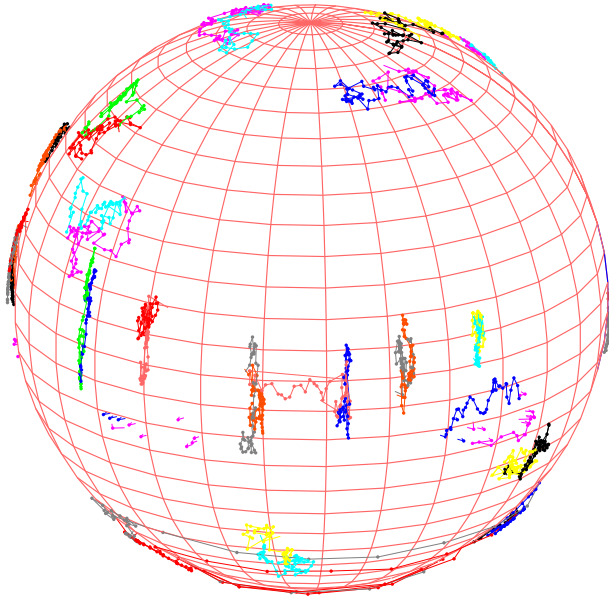
Table 1. Thermodynamic states treated in our simulations: μ (Ry) chemical potential, β (Ry⁻¹) inverse temperature, \bar{N} average number of particles, \bar{r}_s average value of r_s , e_K (Ry) kinetic energy per particle from the thermodynamic estimator as explained in Ref. 28, and e_V (Ry) potential energy per particle. The other quantities were introduced in the main text. We chose length in Bohr radius' units and energy in Rydberg's units. We chose M such as to have $\tau = 0.01$ or less in all cases except case A where we have $\tau = 0.02$.

Case	M	μ	a/a_0	β	\bar{N}	\bar{r}_s	Γ	Θ	e_K	e_V
A	2000	4	5	40	15.03(3)	1.29	62.0	0.261	24.9(3)	2.67(3)
B	500	8	5	5	20.80(8)	1.10	9.12	1.51	48.97(4)	3.857(6)
C	100	10	5	1	29.2(2)	0.925	2.16	5.38	48.5(2)	6.08(5)
D	50	8	5	1/2	31.0(1)	0.898	1.11	10.1	47.84(6)	6.43(3)
E	10	-13	5	1/10	61.8(3)	0.636	0.314	25.4	51(1)	12.83(6)
F	2	-300	5	2/100	58.9(1)	0.651	6.14×10^{-2}	133	61(4)	11.86(2)
G	2	-250	5	0.015	48.00(3)	0.722	4.16×10^{-2}	218	-9(4)	9.412(5)
H	100	4	10	1	35.3(2)	1.68	1.19	17.8	-38(36)	3.90(2)
I	100	0	20	1	50.5(4)	2.81	0.711	49.8	42(3)	3.02(3)
L	100	-8	200	1	17.7(2)	47.5	4.21×10^{-2}	1.42×10^4	45(3)	0.118(1)

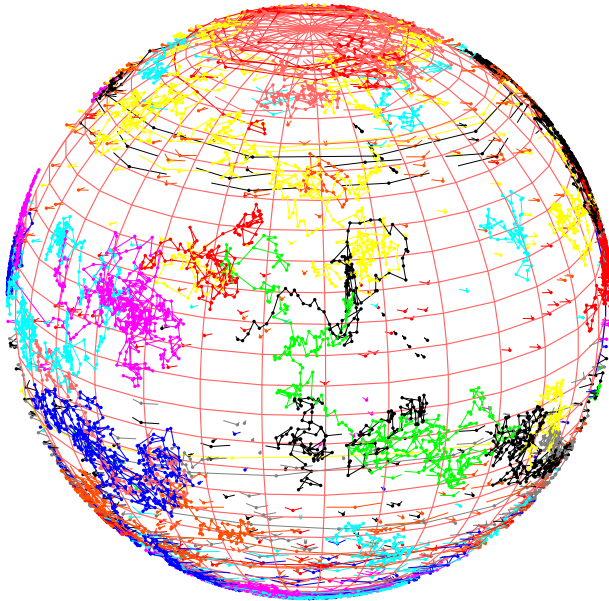
table we see how the potential energy per particle diminishes as the density of the system decreases.

In Fig. 1 we show a snapshot of the macroscopic path during an equilibrated simulation of cases B and C of Table 1. We see how the particles tend to cover the sphere surface isotropically. As it should be since there is nothing able to break the symmetry. Regarding the paths configuration we see immediately that the ones in case B, at lower temperature, are more extended than the ones in case C, at higher temperature, in agreement with the fact that the de Broglie thermal wavelength, the size of a path in absence of interactions, is bigger in case B. We can distinguish between several kinds of conformations. There are the localized paths and the un-localized path covering a large portion of the sphere surface. Paths tend to avoid the poles at low temperature. They tend to wind around the sphere running along the parallels in proximity of the poles and to run along the meridians in proximity of the equator. This is because these are the paths favored by the kinetic-action which is expressed in terms of the square of the geodesic distance of Eq. (4) which, unlike the Euclidean distance, is homogeneous only in the azimuthal angle, the q^2 local coordinate, but not in the polar angle, the q^1 local coordinate. At lower temperature, when the path size increases, the worm diffuses more and we can have paths covering a larger part of the sphere with longer links between two beads. If we rotate the sphere moving its \hat{z} axis, the paths configuration will also rotate.

In Fig. 2 we show the radial distribution function for the cases shown in Table 1. Note that here we are plotting against the Euclidean distance instead of the geodesic one so the value of $g(r)$ on the diameter is at $r = a\sqrt{2}$, the top value is at $r = 0$, and the antipodal value is at $r = 2a$. We then see the effect of curvature on the Coulomb and Fermi hole near contact as they evolve by increasing the temperature. The extent of the Coulomb and Fermi hole at the lowest temperature amounts to roughly 2.5 Bohr's radii. In the limit of very high temperature, the radial distribution



(a)



(b)

Fig. 1. (Color online) Snapshot of the macroscopic path during the simulation of case C in Table 1 in the top panel and case B in Table 1 in the bottom panel. The different worms have different colors. Some paths penetrate through the surface of the sphere and appear as broken links.

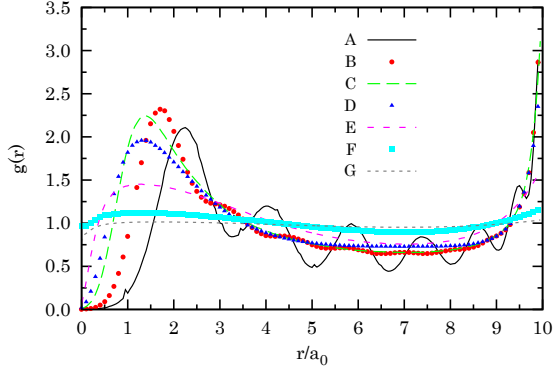


Fig. 2. (Color online) The radial distribution function for the spinless fermion plasma on the sphere of radius $a = 5a_0$ at an inverse temperature β and a chemical potential μ for the cases A-G shown in Table 1.

function tends to the constant function everywhere equal to unity (see case G of Table 1). Another feature of the radial distribution function is the first peak which is produced due to the Pauli exclusion principle, responsible for the Fermi hole, for the Coulomb repulsion, responsible for the Coulomb hole, and for the temperature effect which tends to make particles bump one on the other. From Fig. 2 we clearly see how at small Θ , when the Pauli exclusion becomes strong, the peak tends to shift at larger distances. At very high Θ , the Pauli exclusion becomes very weak and the Fermi hole tends to disappear. Curiously enough the height of the first peak, the probability that sitting on a particle we find one in its neighborhood, is lower than the antipodal value, probability of finding a particle to the particle antipodes. The first peak height and the antipodal value have a nonmonotonic behavior with temperature. Since there are no attractions in the pair-potential, we only observe oscillations in the radial distribution function at very low temperature.

In Fig. 3 we show the radial distribution function of the plasma at the inverse temperature $\beta = 1 \text{ Ry}^{-1}$ on spheres of different diameters and with roughly equal average number of particles, as shown in Table 1 for cases C, H, I and L. Case L corresponds to a sphere of the diameter of 20 nanometers and still presents the Coulomb and Fermi hole. We can see that, as the diameter increases and the density decreases, the first peak height increases. This had to be expected in view of the fact that the system in the semi-quantal regime will tend to crystallize as the density decreases. The peak height tends to become bigger than the antipodal value.

We always worked with no more than 65 electrons which could correspond to the π conduction electrons of the carbon atoms in the graphene sphere. So, the spheres should be made by 10–100 C atoms. The same order of magnitude as in fullerenes where the smallest buckyball cluster is C_{20} and the most common is the buckminsterfullerene C_{60} . Here we are not taking care of the fact that, in graphene, at the Dirac point, electrons have zero effective mass. These graphinos should have a relativistic Hamiltonian rather than the nonrelativistic one we used in Eq. (6).

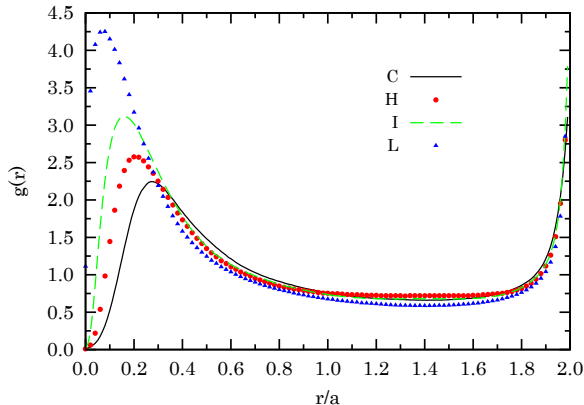


Fig. 3. (Color online) The radial distribution function for the spinless fermion plasma on the sphere of different radii at an inverse temperature $\beta = 1 \text{ Ry}^{-1}$ and a chemical potential μ for the cases shown in Table 1.

4. Conclusions

We simulated a one-component spinless fermion plasma at finite, nonzero, temperature on the surface of a sphere. The Coulomb interaction is e^2/r with r the Euclidean distance between the two electrons of elementary charge e . Here we could as well have chosen instead of r the geodesic distance, s , within the sphere. We used a new implementation of the restricted fixed nodes path integral identity within the worm Monte Carlo algorithm. This gives us an approximated numerical solution of the many-body problem. The exact solution cannot be accessed due to the fermion sign catastrophe. Impenetrable indistinguishable particles on the surface of a sphere admit, in general, anyonic statistics. Here we just project the larger braid group onto the permutation group and choose the fermion sector for our study.

The path integral Monte Carlo method chosen uses the primitive approximation for the action which could be improved for example by the use of the pair-product action.²⁸ The restriction is carried on choosing as the trial density matrix the one of ideal free fermion. This choice would return an exact solution for the simulation of ideal fermions but it furnishes just an approximation for the interacting coulombic plasma.

Our results extend to the quantum regime the previous nonquantum results obtained for the analytically exactly solvable plasma on curved surfaces^{37–42} and for its numerical Monte Carlo experiment.⁴³ Here we just study the geometry of the sphere leaving the more complex surfaces with a nonconstant curvature to a further study. As is shown by the snapshot of the macroscopic path, the configuration space appears much more complicated than in the classical case (see Figs. 5 and 6 of Ref. 43). A first notable phenomena is that whereas the particles distribution is certainly isotropic the paths conformation is not, with beads distributed in such way to avoid the poles at low temperature. Some paths tend to wind around the sphere

running along the parallels in proximity of the poles, others to run along the meridians in proximity of the equator. This is a direct consequence of the coordinate dependence of the variance of the diffusion. If we rotate the sphere the path configuration will also rotate with the sphere. We have several kinds of worms conformations. At high and low temperature: the localized ones, those winding around the sphere along parallels, and those penetrating through the surface of the sphere, at low temperature, the unlocalized ones distributed over a larger part of the surface with long links between the beads of the path.

The structure of the plasma on the sphere reveals how the curvature influences the Coulomb and Fermi holes as they evolve in temperature and density. In particular we observe a monotonic increase of the extent of the Fermi hole as the temperature diminishes. Our analysis shows how the probability of finding a particle nearby another particle is lower than the probability of finding a particle at the antipodes unless for spheres of large diameter. At a higher degeneracy parameter the Pauli exclusion effect becomes less important and the Fermi hole tends to disappear. In the high temperature limit the particles will tend to cover the sphere more uniformly. Decreasing the surface density at fixed low temperature the first peak of the radial distribution function grows monotonically in height, tends to become bigger than its antipodal value, and shifts at smaller distances.

Our computer experiment could be used to predict the properties of a metallic spherical shell, as for example a spherical shell of graphene. Today we assisted the rapid development of the laboratory realization of graphene hollow spheres with many technological interests like the employment as electrodes for supercapacitors and batteries, as superparamagnetic materials, as electrocatalysts for oxygen reduction, as drug deliverers, as a conductive catalyst for photovoltaic applications. Of course, with simulation we can access the more various and extreme conditions otherwise not accessible in a laboratory.

A possible further study would be the simulation of the neutral sphere where we model the plasma of electrons as embedded in a spherical shell that is uniformly positively charged in such a way that the system is globally neutrally charged. This can easily be done by changing the Coulomb pair-potential into $e^2/r \rightarrow e^2(1/r - 1)$. In the $a \rightarrow \infty$ limit, this would reduce to the Wigner Jellium model which has been receiving much attention lately, from the point of view of a path integral Monte Carlo simulation.¹⁻⁸ Alternatively, we could study the two-component plasma on the sphere as has recently been done in the tridimensional Euclidean space.⁴⁴ Another possible extension of our work is the realization of the simulation of the full anyonic plasma on the sphere taking care appropriately of the fractional statistics and the phase factors to append to each disconnected region of the path integral expression for the partition function. This could become important in a study of the quantum Hall effect by placing a magnetic Dirac monopole at the center of the sphere.^{13,14} Also the adaptation of our study to a fully relativistic Hamiltonian could be of some interest for the treatment of the Dirac points graphinos.

Acknowledgments

I would like to dedicate this work to my daughter Alice and to my wife Laure without whose support all this could not have been accomplished. I would like to acknowledge relevant discussions with Saverio Moroni whose comments and suggestions have been invaluable through the whole creation of the work.

References

1. E. W. Brown, B. K. Clark, J. L. DuBois and D. M. Ceperley, *Phys. Rev. Lett.* **110**, 146405 (2013).
2. E. Brown, M. A. Morales, C. Pierleoni and D. M. Ceperley, in *Frontiers and Challenges in Warm Dense Matter*, ed. F. Graziani *et al.* (Springer, 2014), pp. 123–149.
3. T. Dornheim, S. Groth, T. Sjostrom, F. D. Malone, W. M. C. Foulkes and M. Bonitz, *Phys. Rev. Lett.* **117**, 156403 (2016).
4. T. Dornheim, S. Groth, T. Schoof, C. Hann and M. Bonitz, *Phys. Rev. B* **93**, 205134 (2016).
5. S. Groth, T. Schoof, T. Dornheim and M. Bonitz, *Phys. Rev. B* **93**, 085102 (2016).
6. S. Groth, T. Dornheim, T. Sjostrom, F. D. Malone, W. M. C. Foulkes and M. Bonitz, *Phys. Rev. Lett.* **119**, 135001 (2017).
7. F. D. Malone, N. S. Blunt, E. W. Brown, D. K. K. Lee, J. S. Spencer, W. M. C. Foulkes and J. J. Shepherd, *Phys. Rev. Lett.* **117**, 115701 (2016).
8. V. S. Filinov, V. E. Fortov, M. Bonitz and Z. Moldabekov, *Phys. Rev. E* **91**, 033108 (2015).
9. A. Lerda, *Anyons. Quantum Mechanics of Particles with Fractional Statistics*, Lecture Notes in Physics (Springer-Verlag, Berlin Heidelberg, 1992).
10. C. T. Prieto, *J. Phys. Conf. Ser.* **175**, 012014 (2009).
11. H. R. Lee, *J. Korean Phys. Soc.* **34**, S189 (1999).
12. M. Bergeron and G. Semenoff, *Ann. Phys.* **245**, 1 (1996).
13. V. Melik-Alaverdian, N. E. Bonesteel and G. Ortiz, *Phys. Rev. Lett.* **79**, 5286 (1997).
14. V. Melik-Alaverdian, G. Ortiz and N. E. Bonesteel, *J. Stat. Phys.* **104**, 449 (2001).
15. A. Rashid and M. Yusoff, *Graphene-Based Energy Devices* (Wiley-VCH, Weinheim, 2015).
16. A. Tiwari and M. Syväjärvi, *Graphene Materials: Fundamentals and Emerging Applications* (Scrivener Publishing, Massachusetts, 2015).
17. P. Guo, H. Song and X. Chena, *J. Mater. Chem.* **20**, 4867 (2010).
18. J. Cao, Y. Wang, P. Xiao, Y. Chen, Y. Zhou, J.-H. Ouyang and D. Jia, *Carbon* **56**, 389 (2013).
19. L. Wu, H. Feng, M. Liu, K. Zhang and J. Li, *Nanoscale* **5**, 10839 (2013).
20. Q. Shao, J. Tang, Y. Lin, F. Zhang, J. Yuan, H. Zhang, N. Shinyaa and L.-C. Qinc, *J. Mater. Chem. A* **1**, 15423 (2013).
21. Y. Zhao, M. Chen and L. Wu, *Nanotechnology* **27**, 342001 (2016).
22. J. S. Cho, J.-K. Lee and Y. C. Kang, *Sci. Rep.* **6** (2016).
23. D. Hao, C. Xuefen, Q. Liangdong and Z. Xiaohui, *Rare Met. Mater. Eng.* **45**, 1669 (2016).
24. W. Huang, S. Ding, Y. Chen, W. Hao, X. Lai, J. Peng, J. Tu, Y. Cao and X. Li, *Sci. Rep.* **7** (2017).
25. E. Bi, H. Chen, X. Yang, F. Ye, M. Yin and L. Han, *Sci. Rep.* **5** (2017).
26. R. Fantoni, *J. Stat. Mech.* 10024 (2012).
27. L. S. Schulman, *Techniques and Applications of Path Integrals* (John Wiley & Sons, 1981).

28. D. M. Ceperley, *Rev. Mod. Phys.* **67**, 279 (1995).
29. D. M. Ceperley, *J. Stat. Phys.* **63**, 1237 (1991).
30. D. M. Ceperley, in *Monte Carlo and Molecular Dynamics of Condensed Matter Systems*, ed. K. Binder and G. Ciccotti (Editrice Compositori, Italy, 1996).
31. N. V. Prokof'ev, B. V. Svistunov and I. S. Tupitsyn, *J. Exp. Theor. Phys.* **87**, 310 (1998).
32. M. Boninsegni, N. Prokof'ev and B. Svistunov, *Phys. Rev. Lett.* **96**, 070601 (2006).
33. M. Boninsegni, N. V. Prokof'ev and B. V. Svistunov, *Phys. Rev. E* **74**, 036701 (2006).
34. R. Fantoni, *Eur. Comp. Phys. Comm.* (2018), in preparation.
35. R. Fantoni and S. Moroni, *J. Chem. Phys.* **141**, 114110 (2014).
36. J. H. Los, K. V. Z. and M. I. Katsnelson and A. Fasolino, *Phys. Rev. B* **91**, 045415 (2015).
37. R. Fantoni, B. Jancovici and G. Téllez, *J. Stat. Phys.* **112**, 27 (2003).
38. R. Fantoni and G. Téllez, *J. Stat. Phys.* **133**, 449 (2008).
39. R. Fantoni, *J. Stat. Mech.* 04015 (2012).
40. R. Fantoni, *J. Stat. Mech.* 10024 (2012).
41. R. Fantoni, *J. Stat. Phys.* **163**, 1247 (2016).
42. R. Fantoni, *Physica A* **477C**, 187 (2017).
43. R. Fantoni, J. W. O. Salari and B. Klumperman, *Phys. Rev. E* **85**, 061404 (2012).
44. R. Fantoni, *Int. J. Mod. Phys. C* **29**, 1850028 (2018).